RESEARCH ARTICLE

ADVANCED OPTICAL MATERIALS
www.advopticalmat.de

Realization of Secure Robotic Brain Via Programmable Metasurface with Robust High-Order BIC

Xiuyu Wang, Xiaoman Wang, Qun Ren, Jianwei You,* Kaiwen Zou, Boxiang Yang, Zhihao Lan, Liu He, Wei E. I. Sha, and Jianquan Yao**

Terahertz waves can be widely used for short-range communication in complex indoor environments and non-destructive object detection applications. Metasurfaces are widely used in terahertz sensing and communication devices because they can modulate terahertz waves in multiple dimensions. Metamaterial robot brain can utilize metasurfaces' powerful direct modulation ability to achieve sensing and communication functions. The metasurface devices realized based on Dynamic Heterogeneous Redundancy (DHR) architecture can improve the confidentiality and security of terahertz wave wireless communication. While the intrinsic ohmic loss and quality factor of usual metallic metamaterials are usually low, the concept of bound states in the continuum (BIC) has been proposed for stronger terahertz-matter interactions. Among them, high-order BICs are of interest because of their strong robustness to structural defects. Therefore, an aluminium-graphene hybrid metasurface with high-order BIC is proposed. We have the principle of excitation of high-order BICs is investigated and creatively proposed with high robustness realized using the magnetical EIT effect. The robustness of the high-order BIC is also utilized to design security hardware based on DHR architecture. The designed secure hardware can satisfy the demand for an intelligent robotic brain to the internal terahertz wave confidential wireless communication.

1. Introduction

Terahertz waves are characterized by distinct properties, including high bandwidth, low energy consumption, non-ionization, and coherence.[1,2] So, terahertz waves can penetrate obstacles such as walls and furniture, enabling short-distance communication between devices. Terahertz waves also have non-ionizing and coherent properties, which will not damage the detected material's internal structure and intrinsic properties and cause any harm to the human body. Therefore, terahertz waves can be widely used for short-distance communication between indoor devices and daily health monitoring as well as in combination with integrated spectroscopy to realize a new generation of optoelectronic devices used for fields such as nanomedicine, high-speed communication, and industrial non-destructive quality testing.[3–9]

Metasurfaces are capable of complex wavefront modulation of terahertz

X. Wang, X. Wang
Tianjin Key Laboratory of Imaging and Sensing Microelectronic Technology
School of Microelectronics
Tianjin University
Tianjin 300072, China

X. Wang
Purple Mountain Laboratories
Nanjing 211100, China

Q. Ren, K. Zou, B. Yang
School of Electrical and Information Engineering
Tianjin University
Tianjin 300072, China
E-mail: renqun@tju.edu.cn

J. You
State Key Laboratory of Millimeter Waves
School of Information Science and Engineering
Southeast University
Nanjing 210096, China
E-mail: jvyou@seu.edu.cn

Z. Lan
Department of Electronic and Electrical Engineering
Faculty of Engineering Sciences
University College London
London WC1E7JE, UK

L. He, J. Yao
Key Laboratory of Opto-Electronics Information Technology (Tianjin University)
Ministry of Education
School of Precision Instruments and Opto-Electronics Engineering
Tianjin University
Tianjin 300072, China
E-mail: jqyao@tju.edu.cn

W. E. I. Sha
Key Laboratory of Micro-Nano Electronic Devices and Smart Systems of Zhejiang Province
College of Information Science and Electronic Engineering
Zhejiang University
Hangzhou 310027, China

The ORCID identification number(s) for the author(s) of this article can be found under https://doi.org/10.1002/adom.202401611

DOI: 10.1002/adom.202401611

waves.[10–12] Metallic metasurfaces are generally suitable for terahertz frequency communication scenarios.[13–15] Due to their artificially tunable resonance frequencies and operation at subwavelength scales, metasurface-based terahertz sensing and communication devices hold great promise.[16–19] Metasurface robots can utilize the power of metasurfaces in direct modulation to detect indoor environments without violating private information.[20,21] Moreover, highly confidential wireless communication in terahertz waves between the robot brain and the robot limbs can be realized by using metasurfaces.[22] Using Dynamic Heterogeneous Redundancy (DHR) architecture, the metasurface device can obtain more reliable, available, and trustworthy endogenous security functions to realize the confidentiality and security of terahertz wave wireless communication inside the intelligent robot (Supporting Information).

Metallic metasurfaces typically have low-quality factors because metallic radiative losses reduce the quality(Q) factor and, thus, the efficiency of light-matter interactions.[23–26] Bound states in a continuum (BICs) can be used to achieve higher-Q factors metallic metasurfaces.[27,28] BICs are trapped modes located in the radiation continuum region of the energy spectrum.[29,30] Theoretically, BICs have an infinite radiative quality factor but cannot be excited by incident waves.[31–33] However, in the neighborhood of the parameter space of the BIC, quasi-BICs can be excited by incident waves because they do not satisfy the orthogonality condition for resonant states.[34,35] Moreover, the quality factor of the quasi-BIC resonant states is considerably improved, which is essential for developing the devices.[36,37] The merging BIC has attracted attention due to its strong robustness against structural asymmetry. However, merging BIC primarily occurs in photonic crystal slab and requires precise structural parameter adjustments and multidimensional symmetries to merge multiple BICs.[38]

In 2015, Prof. Meng Fanyi's group at the Harbin Institute of Technology published a study on the EIT phenomenon in magnetic metasurfaces, demonstrating that magnetic resonance excitation can excite reverse currents with quasi-BIC features without impaired symmetry.[39] However, the study then mainly utilized z-direction magnetic field excitation with the direction of incidence along the y-axis. Limited by its focus on magnetic resonance excitation, the study did not further explore quasi-BIC phenomena. In recent years, some studies have shown that the dark mode coupling mechanism of the classical EIT effect enables an exotic and straightforward excitation of surface plasmons in a metasurface system.[40] Among them, a study by Shah Nawaz Burokur et al. at the University of Paris Nanterre proposed direct dark mode excitation of a metasurface based on a single folding line, but since the study was limited to the excitation of the dark modes by the linear resonator itself, its straight-line high-order BIC excitation existed only in the hypothesis and was not successfully excited.[41] Building upon these, we propose high-order BICs that can be realized in metasurfaces. High-order BICs share similarities with merging BICs, arising from the merging of two BICs with overlapping spectral positions, and enhancing robustness against resonant scattering losses due to structural defects. Nevertheless, there is currently a lack of research on achieving robust BIC excitations in metallic metasurfaces.

Therefore, this paper proposes an aluminium-graphene hybrid metasurface consisting of two metal cut wires (CWs) and a split-ring resonator (SRR). This metasurface can realize the switching modulation of multiple resonances based on the symmetry-protected BIC. We conducted numerical simulation research on the metasurface using electromagnetic simulation software and explored the potential mechanism of the magnetic EIT effect of multiple resonances. In addition, we creatively propose the principle of the excitation of high-order BICs realized using the magnetic EIT effect and investigate the robustness of the excited high-order BICs. A security hardware design based on DHR architecture is realized by utilizing the robustness of the high-order BIC and by adding a feedback mechanism. The designed secure hardware can satisfy the demand for an intelligent robotic brain to detect the environment and internal terahertz wave confidential wireless communication. The high-order BIC excitation method and its resonant valley with elevated robustness can provide broader prospects for terahertz sensing and communication applications.

2. Results and Methods

In order to realize a multi-channel modulation with high-Q factor, we designed an aluminum-graphene hybrid metasurface. **Figure 1** shows the structure of the metasurface and the transmittance results. The metasurface cell consists of two metal cut wires(CWs) and a split-ring resonator(SRR) made of aluminum and graphene underneath, where one arm of the metal SRR breaks the symmetry, and the gap is filled by graphene, as shown in Figure 1a. The period of the metasurface is 100 μm. The length of the metal CW is $L = 85$ μm, and the width is $w = 5$ μm. The outer length of the SRR is $ly = 60$ μm, the outer width is $lx = 40$ μm, the size of the gap is $d = 5$ μm, the degree of symmetry breaking is $br = 20$ μm, and the distance between the CWs and the SRR is $s = 5$ μm. The metasurface structure consists of a 500-μm-thick high-resistive silicon substrate with a 200-nm-thick metal layer above it and a single-layer graphene patch.

Due to technical constraints, we fabricated a set of pure metal metasurfaces on a high-resistance silicon wafer using standard lithography, which was used to approximate the simulation of Al-graphene hybrid metasurfaces at different Fermi levels. We have characterized the transport response of the metasurface using THz time-domain spectroscopy, the results of which are shown in Figure 1. In the case of both SSR and ASR structures, we observe a slight discrepancy concerning the linewidth of sharp resonance. This discrepancy is mainly due to the limited time window of our measurements, which results in a limited spectral resolution after the fast Fourier transform (FFT), so sharp spectral features cannot be shown particularly accurately. In addition, we performed simulations using the finite element method (FEM) to characterize the transmission response of this metasurface.

We simulated the transmission spectrum of the metasurface using COMSOL. In the simulation, we set the port type to periodic and the periodicity condition was set to be continuous. The relative permittivity of the substrate material, high-resistance silicon, was set to 17, and the aluminum material was set to have a conductivity of 3.67×10^6 using the transition boundary condition approach. Research has shown that by adjusting the geometric parameters of the resonant structure, it is possible to

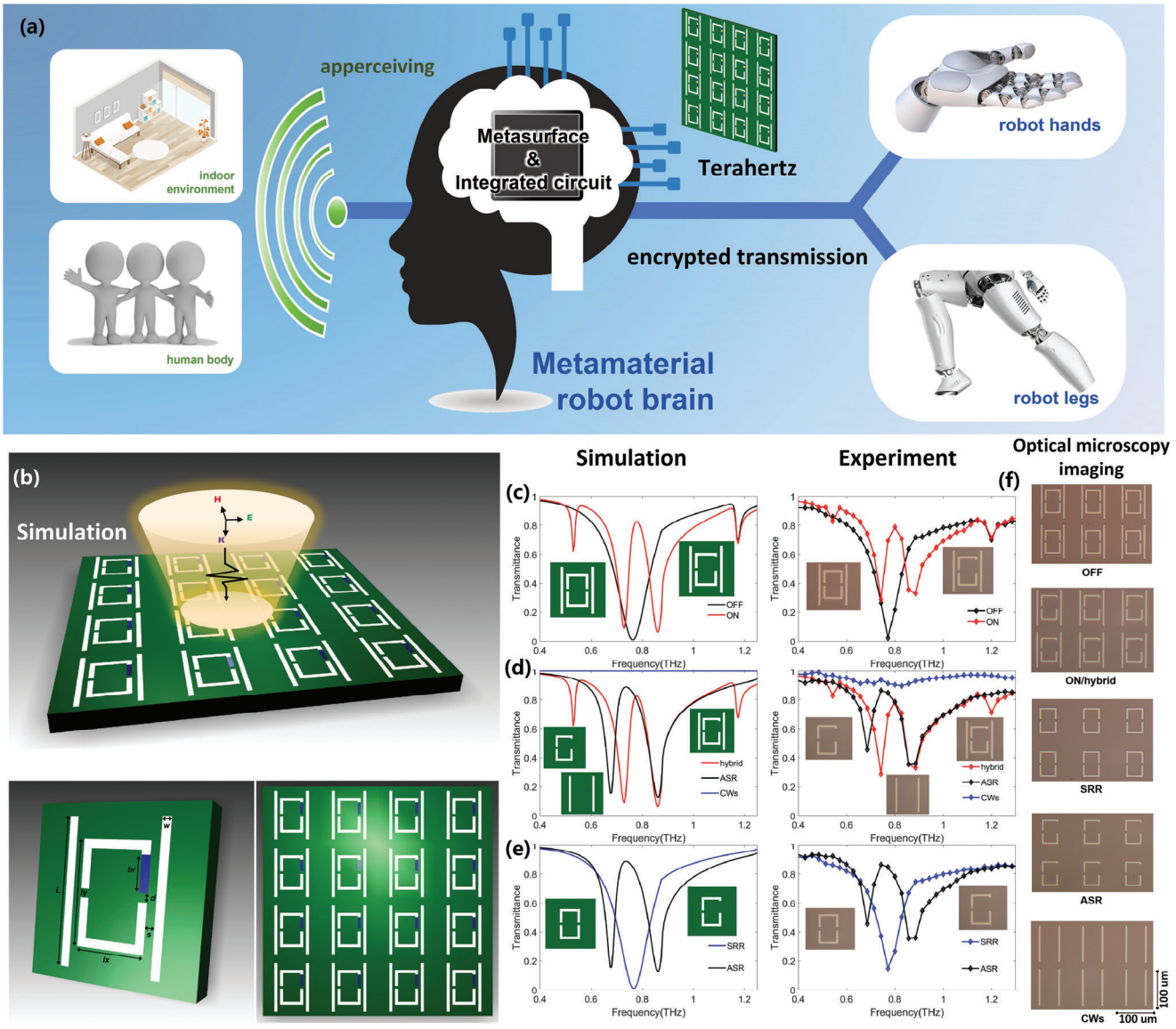

Figure 1. Numerical study of quasi-BICs induced by different symmetric-break. The transmission spectrum for the metasurface of different cases: a) the case of symmetric failure of SRR (bright mode) of the intact metasurface, b) the case of symmetric failure of the exteinnernal CWs (dark mode) of the intact metasurface, c) the case of symmetric failure of individual rings, respectively. And (d), (e), and (f) are the corresponding color maps for different cases of (a), (b), and (c). g) 3D transmission spectrum under the condition cases a. (h), (i), (j), and (k) are the corresponding calculated Q values for BIC1, BIC2, BIC3, and BIC4. The energy band structure of the BIC calculated at different frequencies are shown in inset. The BIC we studyed appears at the Γ point in the first Brillouin zone with a high Q-factor.

tune the resonant frequency, modulation depth, and linewidth of Fano resonance within a limited range.[42–45] Considering the tunability and flexibility of programmable metasurfaces in various practical applications, if an active material-such as semiconductor, graphene, VO_2, or liquid crystal-is integrated into the metasurface array, Fano resonance will achieve precise active control on additional levels with externalstimulation.[46–48] Graphene is a tunable optical material with flexible tunability.[49,50] The tuning of graphene Fermi energy levels can be realized by adding electrodes to the graphene layer to regulate the applied gate voltage, in which the size of the bias source and the bias line necessary are tiny, and the effect on the optical properties of the metasurface is negligible. The conductivity of graphene can be expressed as follows[51]:

$$\sigma \approx \sigma_{intra} = \frac{je^2 E_F}{(\omega + j\tau^{-1})\pi\hbar^2} = \frac{je^2 V_F \sqrt{\pi\alpha V_g}}{(\omega + j\tau^{-1})\pi\hbar} \quad (1)$$

where σ is the conductivity corresponding to the in-band jump, ω is the angular frequency of the terahertz wave, the charge of an electron is e, t is the carrier relaxation lifetime, $\hbar$ is the Planck constant, E_F is the Fermi energy level, $V_F = 10^6 m/s$ is the Fermi velocity and $a = 9 \times 10^6 / m^2 V$ is a capacitance constant. By

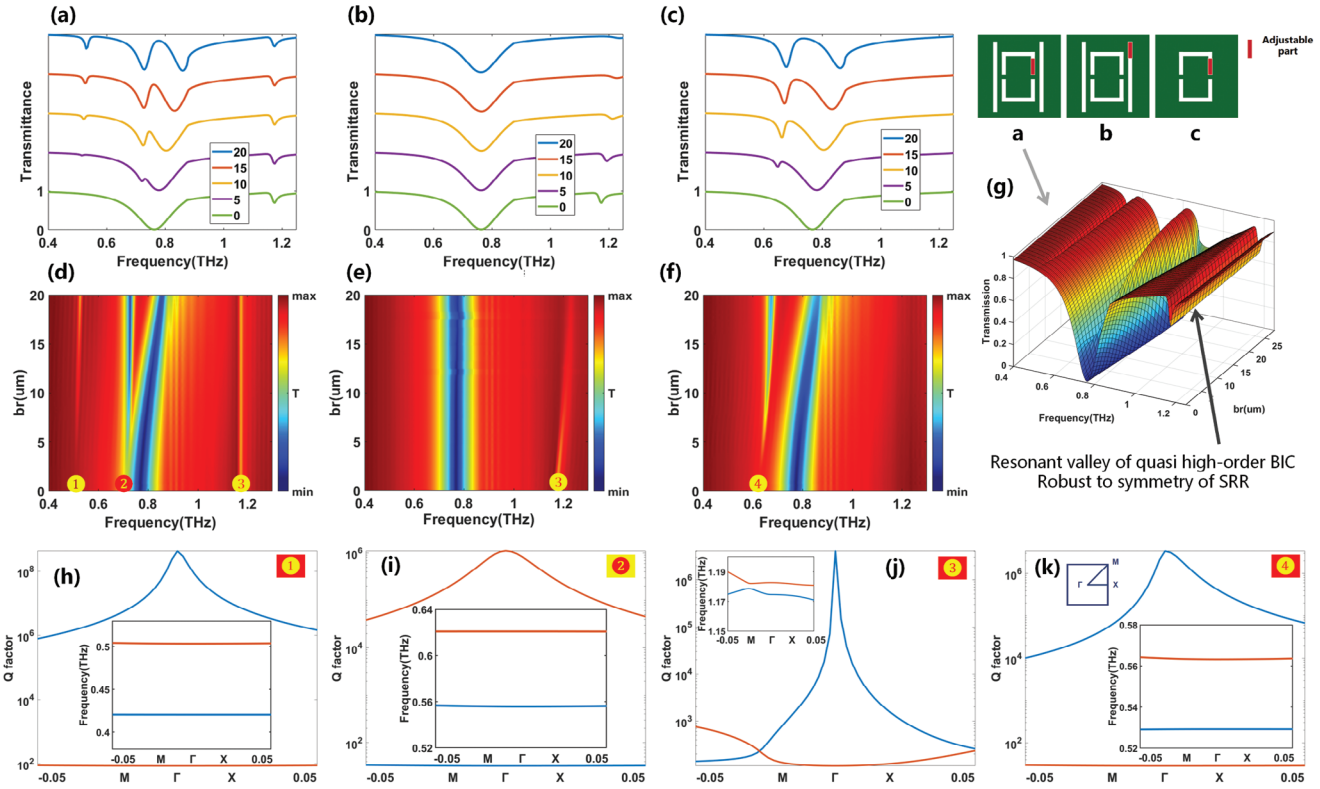

Figure 2. Numerical study of quasi-BICs induced by different symmetric-break. The transmission spectrum color maps and the corresponding calculated Q values for the metasurface of different cases of a) the case of symmetric failure of SRR (bright mode) of the intact metasurface, b) the case of symmetric failure of the exteinnernal CWs (dark mode) of the intact metasurface, c) the case of symmetric failure of individual rings, respectively. The Q-factor and energy band structure of the BIC calculated at different frequencies are shown below (inset). The metal loss is reduced, and the imaginary part of the dielectric constant ϵ is reduced to 10e-6. The quasi-BIC we study appears at the Γ point in the first Brillouin zone with a high Q-factor.

changing the voltage V_g, and then changing the graphene Fermi energy level, and finally changing the electrical conductivity, the regulation of graphene properties can be realized.

A voltage V_g is applied to the graphene patch on the metasurface through the bias line. The graphene with a low applied voltage presents a dielectric-like state. The graphene-metal metasurface is equivalent to the metal metasurface without graphene, corresponding to the metasurface's quasi-BIC state. The metasurface exhibits four distinct resonance peaks at 0.53 THz, 0.73 THz, and 0.86 THz under x-polarization, and a resonance valley at 1.18 THz, as shown in Figure 1d. And when the applied voltage is high, the interaction strength of graphene with terahertz waves is comparable to that of metal with terahertz waves. Graphene can be regarded as a metal equivalent to a completely symmetric all-metal metasurface. Currently, there are only two resonance valleys located at 0.76 and 1.18 THz. Therefore, in our structure, by using an applied voltage to change the state of the graphene patch, we can realize free switching for controlling multiple frequency bands.

In order to elucidate the mechanism of multiband generation in this metasurface, three sets of samples are set up for simulation as shown in **Figure 2**. The results of the transmission spectra for different degrees of symmetry breaking are further analyzed with three different sets of samples. The symmetry-protected BICs in the metasurface are verified by utilizing the fact that the symmetry-protected BICs will have a resonance vanishing phenomenon in the symmetry recovery region.

The results of the first set of samples, in which the parameter of the degree of broken symmetry of the SRR is individually adjusted in the case of complete structural unit, are shown in Figure 2a. Spectral features labeled 1 and 2 with pronounced quasi-BICs become significantly narrower as the asymmetry parameter *br* decreases and disappear entirely at *br* of 0, showing a strong dependence on the *br*. The results of the first set of samples are shown in Figure 2a. Meanwhile, the resonance valley located at 1.18 THz does not change with the change of the asymmetry parameter *br*, indicating that this resonance valley is independent of the degree of breaking in the case of ring breaking. This suggests that the resonance valley corresponding to BIC3 arises from a different cause than the resonance valleys of BIC1 and BIC2.

To further verify the principle of the resonance valleys corresponding to BIC1 and BIC2, the second set of samples consists of separate ASR, as shown in Figure 2b. The resonance valley labeled 4 has a strong dependence on the asymmetry parameter *br* and its phenomenon narrows significantly with the decrease of the *br*, and disappears entirely when *br* is 0. This resonance valley and the corresponding resonance valleys of BIC1 and BIC2 have similar properties, and both are very sensitive to the symmetry of the ring. Since the relative positions of the resonance valleys corresponding to BIC2 and BIC4 and the resonance valley excited

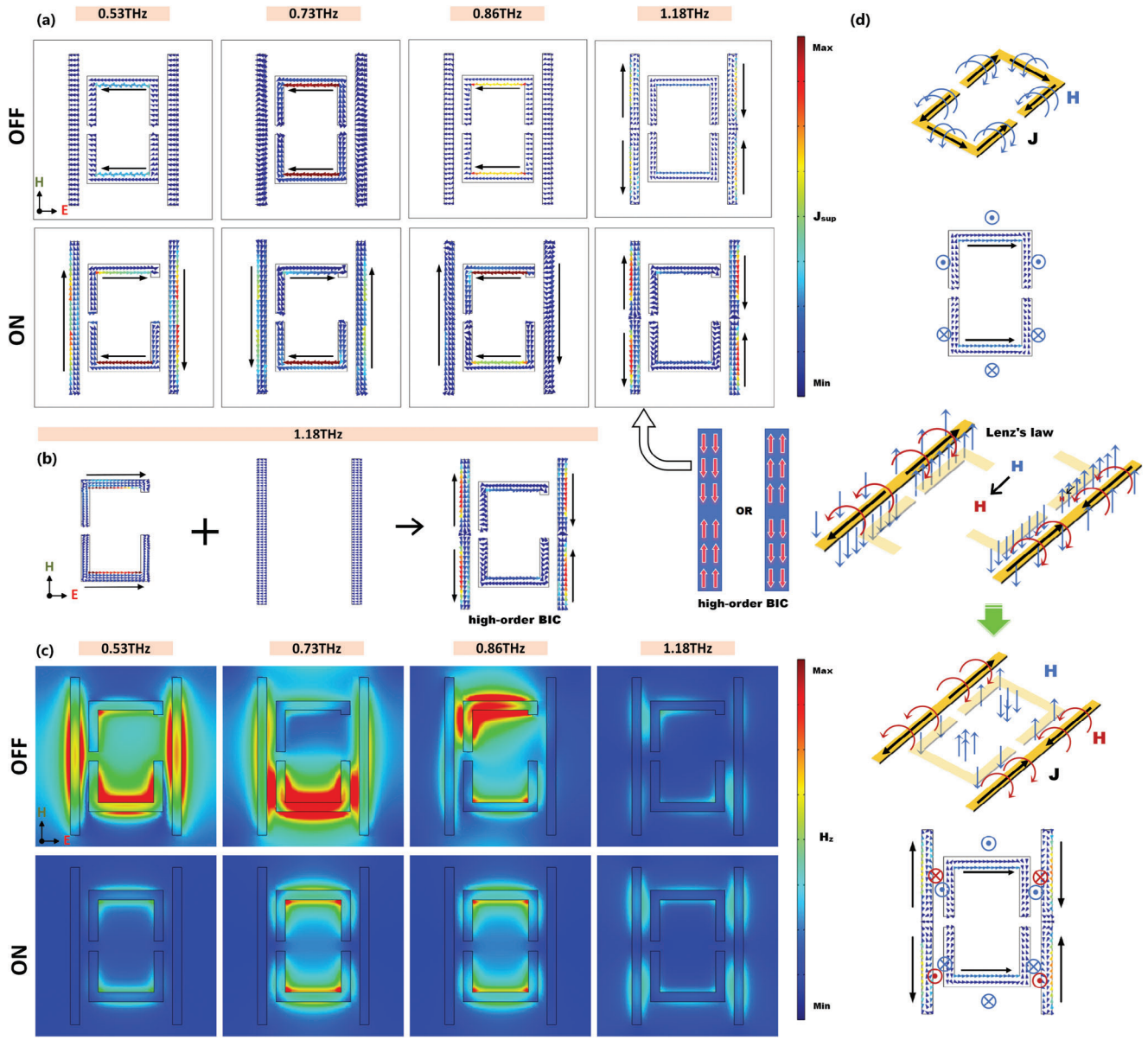

Figure 3. Principle study of high-order BIC states. a) Surface current distribution of the metasurface at different states and frequencies. b) Surface current distribution of individual rings and individual CWss at 1.18 THz frequency. c) Distribution of z-direction magnetic field of the metasurface at different states and frequencies. d) The principle of magnetic excitation of EIT to produce high-order BIC states.

by the dipole located at 0.8 THz are close to each other, it can be hypothesized that both valleys are excited by the symmetry-protecting BIC of the ring itself. Because the asymmetric ring in BIC2 also has some excitation of the doublet, leading to a specific frequency shift from the phenomenon that is BIC4.

Although the BIC1 resonance valley is also sensitive to ring symmetry, it can be inferred from the different electric field distributions from the BIC2 resonance valley that the leading cause of this resonance valley is the SRR and CWs ordinary BIC being excited by the ring asymmetry. Moreover, in order to verify the principle of BIC3, a third set of samples is set up consisting of complete structural units that break the symmetry of the CWs, as shown in Figure 2c. It can be seen that the resonance valley of the BIC labeled 5 in this figure is the same as that of BIC3. In modulating the bilinear symmetry, there is no phenomenon for BIC1 and BIC2, which appear as quasi-BIC features in the first set of samples, indicating that the excitation of these two BICs is unrelated to the CWs symmetry.

In contrast, the resonance valley generated by the excitation of BIC3 fades away as the symmetry-breaking parameter br of the CWs increases, which is opposite to the characterization of the classical symmetry-protected BIC. This indicates that while BIC3 is heavily correlated with the CWs, the reason for its generation is not the direct excitation of the CWs by external terahertz waves. Moreover, **Figure** 3c shows that the CWs alone do not resonate under x-polarized terahertz incident waves, corroborating

this inference. Therefore, the high-order BIC of the symmetric CWs excited by the single SRR should generate the resonance valley. In summary, there are three BICs with different excitation modes in the designed metasurface, among which BIC1 is the classical symmetry-protected BIC with the asymmetric single SRR as the bright mode and the CWs excited as the dark mode, which is dependent on the ring symmetry. BIC3 is a high-order BIC with rings as bright modes and symmetric CWs excited as dark modes by magnetic resonance.

Theoretically, an ideal BIC is characterized by a quality factor that tends to infinity.[52] The intrinsic losses in the metal and the dielectric losses in the substrate cause the BIC to appear in practice as a lossy BIC with a tiny quality factor.[53,54] The energy leakage from the lossy BIC to the port is zero, and the ideal BIC quality factor can be approximated by eliminating the metal loss factor, i.e., by setting the imaginary part of the dielectric constant close to 0. Therefore, the ideal BIC quality factor can be approximated by simplifying the dielectric constant to 10^{-5} to get close to the lossless metal. Thus, it is possible to simplify the imaginary part of the dielectric constant to 10^{-5} to obtain a near-lossless metal by calculating the Q-factor. Figure 2d shows the Q-factor calculated for the metasurfaces near the corresponding frequency using this method, exhibiting that the quasi-BIC calculated Q-factor rises rapidly to a tremendous value at the symmetry point Γ, and the calculated Q-factor is protected by the point Γ. The inset shows the possible eigenmodes in the M-Γ direction near the corresponding frequency.

3. Analysis

3.1. Principle Analysis and Robustness of High-Order BIC Excitation

The surface current distribution with high-order BIC features appears on the CWs at 1.18 THz, which manifests itself as two segments of surface currents with entirely opposite directions, as shown in Figure 3a. Unlike the other three resonance valleys, the CWs have strong currents in both ON and OFF states and excite resonance valleys independent of ring symmetry.

In order to analyze the reason why the high-order BIC modes of the CWs are excited, we simulated the currents at 1.18 THz for the CWs alone and the SRR alone as well, as shown in Figure 3b. It can be seen that the SRR alone can excite the current in the same direction at this frequency. At the same time, the CWs alone will not be excited. Therefore, it can be speculated that both the ring in a bright mode and the wire in a dark mode produce the EIT effect to excite the surface current of the CWs with high-order BIC characteristics. However, the surface current with BIC characteristics excited by the EIT effect is usually a section of surface current with opposite directions. In order to further analyze the reason for the excitation of the CWs with high-order BIC features, we also simulate the z-direction magnetic field of the metasurface.

In the BIC state, the energy transfer of the electromagnetic wave is mainly in the z-axis direction, i.e., the waveprinting vectors are all in the z-axis direction. Thus, the magnetic field is confined to the x-o-y plane. However, in the case of QUASI-BIC, part of the magnetic field is generated outside the x-o-y plane due to energy leakage. Therefore, by monitoring the magnetic field component in the z-axis direction, quasi-BIC and BIC can be easily verified by the energy leakage. As shown in Figure 3c, unlike other frequencies, there is no significant z-direction magnetic field at 1.18 THz regardless of whether the symmetry of the ring is broken, so it is not a quasi-BIC state that is produced but a BIC state. The resonance valleys at 1.18 THz in both symmetric and asymmetric cases, proving that the resonance valleys are not in a symmetry-protected quasi-BIC state, but rather are generated by exciting a quasi-high-order BIC in some other way.

Based on previous studies, we analyze the distribution of BIC-like currents generated in the symmetric case. It can be deduced that the high-order BICs are generated because the isotropic currents in the ring generate a magnetic field perpendicular to the plane of the metasurface that is asymmetric concerning the CWs at 1.18 THz. Due to the inhomogeneous distribution of the magnetic field around the line, the localized flute law excites the current on the CWs to produce a magnetic field against the inhomogeneous field. Since the magnetic resonance in the open ring is much stronger than in the CWs, the open ring is used as a bright resonator and the CWs as a dark resonator. In summary, the resonance valley at 1.18 THz is a magnetically excited Fano phenomenon resulting from the realization of constructive interference by the SRR and the CWs as bright and dark modes, respectively.

In the vicinity of the 1.18 THz frequency, the high-order BIC modes of the CWs can be excited by electromagnetic waves polarized in the X-direction and generate an asymmetric magnetic field perpendicular to the plane of the metamaterial. The SRR cannot be directly excited by the incident wave but by the asymmetric magnetic field in the space between the CWs to produce a current. Thus, this resonance valley is a magnetic EIT phenomenon produced by SRRs and CWs that act as dark and bright modes for destructive and constructive interference. We present the use of magnetic resonance to excite high-order BICs directly. The resonance valleys excited by this method have good robustness to scattering loss from structural defects, providing a new idea for future research on high-order BICs.

3.2. Metasurface Secure Device Realized by Utilizing the Strong Robustness Possessed by High-Order BICs as a Ruling Mechanism

Generally, conventional metallic metasurfaces are limited by the material's relatively fixed electromagnetic parameters. The application of metasurfaces to electromagnetic waves is restricted to sensors, filters, and nonlinear optics. In recent years, programmable metasurfaces, capable of flexibly manipulating electromagnetic properties in channel environments, have attracted considerable attention from the industry upon their appearance. By applying control signals to tunable elements on electromagnetic units, programmable metasurfaces can dynamically control the electromagnetic properties of these electromagnetic units, thus realizing active programmable modulation of space electromagnetic waves in a programmable manner. The hardware architecture of a programmable metasurface consists of three main parts: a reconfigurable electromagnetic surface, a feed system, and a control system. The computer acts as a feeder system to

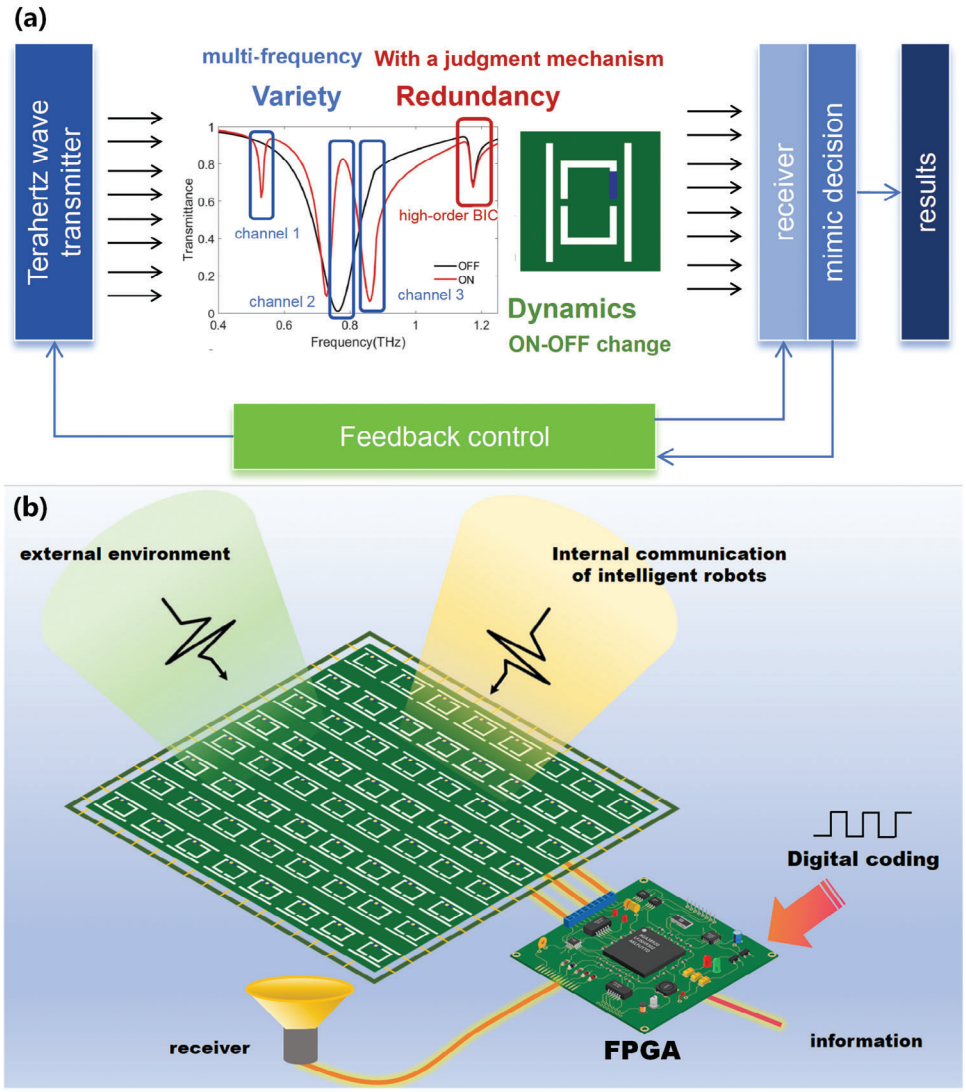

Figure 4. Schematic diagram of a metasurface security device realized using a high-order BIC. a) The principle of realizing a secure device is using the strong robustness that high-order BICs have as an adjudication mechanism. b) Conceptual diagram of the encoded digital metasurface. The transmission coefficient of the metasurface element can be dynamically controlled by applying a control voltage to the graphene patch through the FPGA.

convert the input characters into high-frequency textual information signals. The field-programmable gate array FPGA acts as the control system, and by configuring low-frequency control signals to the graphene-metal metasurface, the electromagnetic properties of graphene can be altered to regulate the high-frequency signals from the feed system dynamically. The Dynamic Heterogeneous Redundancy (DHR) proposed by Wu Jiangxing's team utilizes the principle of complete intersection of DVRs to be able to transform a generalized uncertain perturbation into a security event of differential or common-mode nature in the domain of DVRs that probabilistic tools can describe.[55] If a target object is dynamically diverse and redundant, it can effectively counter any unknown network security or functional security threat, even without prior knowledge. The metasurface devices implemented based on Dynamic Heterogeneous Redundancy (DHR) architecture can obtain more reliable, available, and trustworthy endogenous security features to realize confidential security of terahertz wave wireless communication within intelligent robots.

The principle of complete DVR intersection requires the system to be simultaneously dynamic, variety, and redundant. The metasurface is capable of realizing a model of DVR intersection. Where D (dynamics) is provided by graphene patches that dynamically modulate the resonance valley positions, uncertainty is introduced into the metasurface system. V (variety) is provided by multiple frequency bands, which are non-similar due to the similarity of the principles but are different but not sufficient to meet the heterogeneity criteria. R (redundancy) is where the data from each band corroborates with each other (majority verdict) and utilizes the high-order BIC resonance valleys as a verdict mechanism, which makes the system reliable. On top of this, introducing a feedback mechanism and a policy adjudication mechanism enables the realization of secure hardware against dynamic interference. As shown in **Figure 4**, the

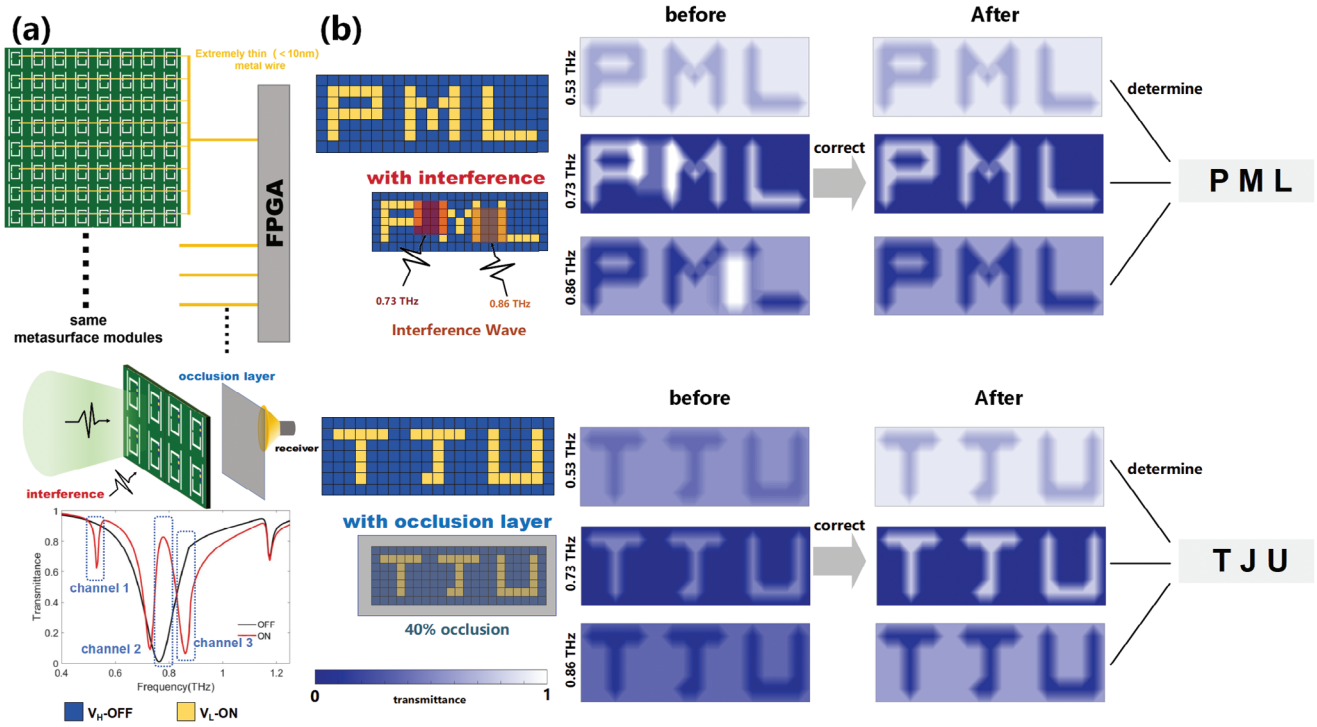

Figure 5. Functional case realized using high-order BIC. a) The principle of the digital display function is realized using the strong robustness of the high-order BIC as the adjudication mechanism. b) Simulation results of digital display with error correction function.

metasurface security device system, which consists of heterogeneity, redundancy, dynamics, adjudication, and feedback control, can maximize the synergy effect of the three elements of "dynamic, diverse, and stochastic" defense. According to previous research, this architecture can solve the problem of external interference in a downscaled manner. This device can meet the information security needs of robotic brains and help develop intelligent robotic brains in the future.

3.3. Digital Display Functions Utilizing Metasurface Safety Devices

The digital display function is used as an example to demonstrate the capabilities of our construction more intuitively. By controlling a Field Programmable Gate Array FPGA with computer programming and changing the state of graphene on the metasurface, our metasurface can realize dynamic display functions, as shown in **Figure 5**.

A voltage V_g is applied externally to the graphene patches. When the graphene-metal metasurface is in the V_H-controlled OFF state and the V_L-controlled ON state, respectively, the transmissions at the resonance frequency at the two states are significantly different at the 0.53, 0.73, and 0.86 THz, as shown in Figure 5. Each graphene-metal structure in the shown metasurface array is considered a pixel. The FPGA can independently control the graphene patches on each pixel. When the graphene structure is connected to a high voltage (V_H) level, the E_F increases to 10 eV, corresponding to being in a completely symmetric BIC state, and the transmission spectrum corresponds to the black curve.

On the contrary, when the structure is connected to a low-level voltage (V_L), the E_F decreases to 0.01 eV. In this case, the structure is equivalent to a symmetry-broken quasi-BIC state, and the transmission spectrum corresponds to a red curve. Different electromagnetic field strength distributions are presented when different pixels have different states, i.e., the image display function is obtained. As shown in the simulation results of dynamic imaging, we have demonstrated the letters at three channels.

With this safety device, an adaptive correction function for the received spectrum can be realized since the actual test needs to require the ratio of the frequency domain spectrum of the metasurface and the frequency domain spectrum of the air to obtain the metasurface's transmission spectrum. The frequency domain spectrum of air is a specific value measured in advance. However, suppose there is localized occlusion or uneven intensity of positively incident terahertz waves during the detection of the metasurface. In that case, the frequency domain spectrum of the metasurface in that part may change and lead to misdetection of the displayed results. For example, if there is localized occlusion or the localized terahertz wave intensity is small, the intensity of the transmitted light corresponding to a high transmission state may be reduced, resulting in a misjudgment of a low transmission state. If the local terahertz wave intensity is significant, the transmitted light intensity corresponding to the low-transmission state may be increased, leading to the misjudgment of the high-transmission state. All of the above situations may lead to errors in the digital display. From the previous results of the transmission spectrum, it can be seen that the

transmittance of the frequencies corresponding to the high-order BICs is permanently stabilized by changing the symmetry of the CWs. Therefore, the symmetry of the graphene patch modulation ring will significantly affect the other resonance valleys without affecting the resonance corresponding to the high-order BIC. The resonance valleys corresponding to high-order BICs always have high robustness, which is the basis for realizing reliable digital display functions using high-order BICs. In summary, uniform calibration can be performed by the transmission situation corresponding to the high-order BIC states to avoid erroneous results due to reasons such as occlusion and terahertz incident wave intensity variations, as shown in Figure 5. By comparing the transmitted light intensity at 1.18 THz, the results can be processed to correct the displayed results adaptively, and an accurate character display can be obtained, which significantly improves the reliability of the digital display and realizes the safe hardware that can avoid the influence of external dynamic electromagnetic wave interference.

4. Conclusion

In this paper, we present an Al-Graphene hybrid metasurface. This metasurface can switch the modulation of multiple resonances based on the symmetry-protected BIC. Numerical simulation studies of the metasurface have been performed using electromagnetic simulation software to investigate the underlying mechanism of the magnetic EIT effect for multiple channel resonances and to demonstrate the existence of multiple BICs. In addition, we creatively present the excitation principle of high-order BICs realized using the magnetic EIT effect and investigate the robustness of the excited high-order BICs. A security hardware design based on a dynamic heterogeneous redundancy architecture is implemented by exploiting the robustness of the high-order BIC and by adding a feedback mechanism. The designed secure hardware can satisfy the requirements of an intelligent robotic brain to detect the environment and conduct internal terahertz wave secrecy wireless communications. Higher-order BIC excitation methods and their highly robust resonant valleys can offer broader prospects for THz sensing and communication applications.

Supporting Information

Supporting Information is available from the Wiley Online Library or from the author.

Acknowledgements

The authors thank the National Natural Science Foundation of China for help identifying collaborators for this work.

Conflict of Interest

The authors declare no conflict of interest.

Data Availability Statement

Data will be made available on request.

Keywords

bound states in the continuum, dynamic heterogeneous redundancy, metasurface, terahertz

Received: June 16, 2024
Revised: August 29, 2024
Published online: October 9, 2024

[1] L. Gao, Q. Cheng, J. Yang, S. Ma, J. Zhao, S. Liu, H. Chen, Q. He, W. Jiang, H.-F. Ma, Q.-Y. Wen, L.-J. Liang, B.-B. Jin, W.-W. Liu, L. Zhou, J.-Q. Yao, P.-H. Wu, T.-J. Cui, *Light: Sci. Appl.* **2015**, *4*, e324.
[2] I. F. Akyildiz, C. Han, Z. Hu, S. Nie, J. M. Jornet, *IEEE Trans. Commun.* **2022**, *70*, 4250.
[3] R. Wang, L. Xu, L. Huang, X. Zhang, H. Ruan, X. Yang, J. Lou, C. Chang, X. Du, *Small* **2023**, *19*, 2301165.
[4] M. Du, J. Zhou, X. Luo, L. Duan, D. Zhang, *Moore and More* **2024**, *1*, 1.
[5] N. Mou, S. Sun, H. Dong, S. Dong, Q. He, L. Zhou, L. Zhang, *Opt. Express* **2018**, *26*, 11728.
[6] Q. Xu, X. Zhang, Y. Xu, C. Ouyang, Y. Li, J. Han, W. Zhang, *Chin. Opt. Lett.* **2018**, *16*, 050002.
[7] X. Lai, Q. Ren, F. Vogelbacher, W. E. Sha, X. Hou, X. Yao, Y. Song, M. Li, *Adv. Mater.* **2022**, *34*, 2107243.
[8] C. Guo, J. Zhang, X. Cai, R. Dou, J. Tang, Z. Huang, X. Wang, Y. Guo, H. Chen, J. Chen, *iMetaOmics* **2022**, e12.
[9] W. Shen, Z. Song, X. Zhong, M. Huang, D. Shen, P. Gao, X. Qian, M. Wang, X. He, T. Wang, S. Li, X. Song, *iMeta* **2022**, *1*, e36.
[10] W. Zhu, M. Jiang, H. Guan, J. Yu, H. Lu, J. Zhang, Z. Chen, *Photonics Res.* **2017**, *5*, 684.
[11] L. Lin, J. Hu, S. Dagli, J. A. Dionne, M. Lawrence, *Nano Lett.* **2023**, *23*, 1355.
[12] T. J. Cui, D. R. Smith, R. Liu, *Metamaterials*, Springer, Berlin **2010**.
[13] N. I. Zheludev, Y. S. Kivshar, *Nat. Mater.* **2012**, *11*, 917.
[14] A. Zeb, F. Li, in *2019 IEEE 11th International Conference on Communication Software and Networks (ICCSN)*, IEEE, Piscataway, NJ **2019**, pp. 332–336.
[15] Y. Chen, X. Wang, F. Ye, P. Lee, B. Hu, *Appl. Phys. B* **2012**, *107*, 771.
[16] J. W. You, Q. Ma, Z. Lan, Q. Xiao, N. C. Panoiu, T. J. Cui, *Nat. Commun.* **2021**, *12*, 5468.
[17] Z. Yu, Y. Tong, H. K. Tsang, X. Sun, *Nat. Commun.* **2020**, *11*, 2602.
[18] W. Cen, T. Lang, Z. Hong, J. Liu, M. Xiao, J. Zhang, Z. Yu, *IEEE Sens. J.* **2022**, *22*, 12838.
[19] T. J. Cui, M. Q. Qi, X. Wan, J. Zhao, Q. Cheng, *Light: Sci. Appl.* **2014**, *3*, e218.
[20] X. Luo, *Natl. Sci. Rev.* **2023**, *10*, nwad064.
[21] H. Zhao, S. Hu, H. Zhang, Z. Wang, H. Dong, P. Del Hougne, T. J. Cui, L. Li, *Natl. Sci. Rev.* **2023**, *10*, nwac266.
[22] X. Bai, S. Tan, S. Mikki, E. Li, T.-J. Cui, *Progress In Electromagnetics Research* **2024**, *179*, 1.
[23] X. Wang, X. Wang, Z. Yao, G. Guo, Y. Jia, Y. He, R. Jin, Y. Lang, J. You, Q. Ren, Q. Xu, W. E. I. Sha, Y. Pang, *Opt. Mater.* **2023**, *143*, 114154.
[24] X. Wang, X. Wang, J. Xin, J. Li, Q. Ren, H. Cai, Y. Lang, Z. Lan, Y. Jia, R. Jin, Y. He, J. W. You, W. E. I. Sha, Y. Pang, *Opt. Commun.* **2023**, *549*, 129834.
[25] L. Huang, S. Li, C. Zhou, H. Zhong, S. You, L. Li, Y. Cheng, A. E. Miroshnichenko, *Adv. Funct. Mater.* **2024**, *34*, 2309982.
[26] K. Koshelev, S. Lepeshov, M. Liu, A. Bogdanov, Y. Kivshar, *Phys. Rev. Lett.* **2018**, *121*, 193903.
[27] X. Zhao, C. Chen, K. Kaj, I. Hammock, Y. Huang, R. D. Averitt, X. Zhang, *Optica* **2020**, *7*, 1548.

[28] Z. Liu, Y. Xu, Y. Lin, J. Xiang, T. Feng, Q. Cao, J. Li, S. Lan, J. Liu, *Phys. Rev. Lett.* **2019**, *123*, 253901.
[29] L. Huang, L. Xu, D. A. Powell, W. J. Padilla, A. E. Miroshnichenko, *Phys. Rep.* **2023**, *1008*, 1.
[30] D. Marinica, A. Borisov, S. Shabanov, *Phys. Rev. Lett.* **2008**, *100*, 183902.
[31] C. W. Hsu, B. Zhen, A. D. Stone, J. D. Joannopoulos, M. Soljačić, *Nat. Rev. Mater.* **2016**, *1*, 16048.
[32] X. Wang, J. Xin, Q. Ren, H. Cai, J. Han, C. Tian, P. Zhang, L. Jiang, Z. Lan, J. You, W. E. I. Sha, *Chin. Opt. Lett.* **2022**, *20*, 042201.
[33] C. Zhou, L. Huang, R. Jin, L. Xu, G. Li, M. Rahmani, X. Chen, W. Lu, A. E. Miroshnichenko, *Laser Photonics Rev.* **2023**, *17*, 2200564.
[34] Y. Cai, Y. Huang, K. Zhu, H. Wu, *Opt. Lett.* **2021**, *46*, 4049.
[35] L. Xu, K. Zangeneh Kamali, L. Huang, M. Rahmani, A. Smirnov, R. Camacho-Morales, Y. Ma, G. Zhang, M. Woolley, D. Neshev, A. E. Miroshnichenko, *Adv. Sci.* **2019**, *6*, 1802119.
[36] Z. Cui, Y. Wang, G. Sun, W. Chen, X. Zhang, K. Zhang, X. Wang, *ACS Appl. Mater. Interfaces* **2024**, *16*, 7631.
[37] Q. Ren, F. Feng, X. Yao, Q. Xu, M. Xin, Z. Lan, J. You, X. Xiao, W. E. Sha, *Opt. Express* **2021**, *29*, 5384.
[38] W. Wang, A. Günzler, B. D. Wilts, U. Steiner, M. Saba, *Adv. Photonics* **2023**, *5*, 056005.
[39] L. Zhu, F. Meng, L. Dong, Q. Wu, B. Che, J. Gao, J. Fu, K. Zhang, G. Yang, *J. Appl. Phys.* **2015**, *117*, 17.
[40] X. Zhang, Q. Xu, Q. Li, Y. Xu, J. Gu, Z. Tian, C. Ouyang, Y. Liu, S. Zhang, X. Zhang, J. Han, W. Zhang, *Sci. Adv.* **2016**, *2*, e1501142.
[41] S. N. Burokur, A. Lupu, A. De Lustrac, *Phys. Rev. B* **2015**, *91*, 035104.
[42] T. Pan, J. Ye, Z. Zhang, Y. Xu, *Opt. Lett.* **2022**, *47*, 3359.
[43] T. Lv, Y. Li, H. Ma, Z. Zhu, Z. Li, C. Guan, J. Shi, H. Zhang, T. Cui, *Sci. Rep.* **2016**, *6*, 23186.
[44] M. F. Limonov, M. V. Rybin, A. N. Poddubny, Y. S. Kivshar, *Nat. Photonics* **2017**, Nature Publishing Group UK London, *11*, 543.
[45] A. E. Miroshnichenko, S. Flach, Y. S. Kivshar, *Rev. Mod. Phys.* **2010**, *82*, 2257.
[46] D. Kang, H. Heo, Y. Yang, J. Seong, H. Kim, J. Kim, J. Rho, *Opto-Electronic Adv.* **2024**, *7*, 230216.
[47] S. Li, X. Zhang, Q. Xu, M. Liu, M. Kang, J. Han, W. Zhang, *Opt. Express* **2020**, *28*, 20083.
[48] X. Wang, X. Wang, Q. Ren, H. Cai, J. Xin, Y. Lang, X. Xiao, Z. Lan, J. You, W. E. Sha, *Front. Nanotechnol.* **2023**, *5*, 1112100.
[49] H. Chen, W. Lu, Z. Liu, M. Geng, *Acs Photonics* **2020**, *7*, 1425.
[50] Q. Ren, J. W. You, N.-C. Panoiu, *IEEE Access* **2020**, *8*, 175753.
[51] M. Fang, Z. Huang, E. Wei, C. M. Soukoulis, *IEEE Trans. Nanotechnol.* **2021**, *20*, 543.
[52] E. P. Wigner, *The collected works of Eugene Paul Wigner: Historical, philosophical, and socio-political papers. Historical and Biographical Reflections and Syntheses*, Springer Science & Business Media, Dordrecht **2013**.
[53] L. Wang, Z. Zhao, M. Du, H. Qin, R. T. Ako, S. Sriram, *Opt. Express* **2022**, *30*, 23631.
[54] S. Chen, Q. Ren, K. Zhang, E. Wei, T. Hao, H. Xu, J. Zhao, Y. Li, *Sens. Actuators, B* **2022**, *355*, 131326.
[55] J. Wu, *Engineering* **2022**, *15*, 179.